

Efficiency of pump absorption in double-clad fiber amplifiers.

II. Broken circular symmetry

Dmitrii Kouznetsov and Jerome V. Moloney

Arizona Center for Mathematical Sciences, Department of Mathematics, University of Arizona, 617 North Santa Rita, Tucson, Arizona 85721

Received February 23, 2001; revised manuscript received November 9, 2001

Absorption of an incoherent pump in a double-clad fiber amplifier is analyzed in the paraxial wave approximation. Different inner cladding shapes are considered. A small spiral distortion of an otherwise circular inner cladding shape is shown to enhance the coupling efficiency significantly relative to other geometries.

© 2002 Optical Society of America

OCIS codes: 140.3510, 060.2320, 060.0060, 060.2270.

1. INTRODUCTION

Double-clad fibers offer an efficient means of coupling the partially coherent light of diode lasers into single-transverse-mode radiation.¹⁻⁴ The absorption of the pump light in the core is almost linear.^{5,6} The efficiency of absorption of the pump light in the core of the double-clad fiber is important for power scaling of double-clad fiber amplifiers. This efficiency is low in the case of an inner cladding with circular symmetry.^{7,8} However, small fluctuations of the index of refraction can significantly increase this coupling.⁹ Effective pump inner-cladding mode mixing takes place in so-called chaotic fibers.^{10,11} For example, the double-truncated circular fiber¹⁰ provides good mixing, approaching the analytical estimation for the effective absorption rate $\mathcal{K}_{\text{eff}} = \mathcal{K}_0 s / (S + s)$, where \mathcal{K}_0 is the local absorption rate in the core and s and S are areas of the cross section of core and cladding, respectively. However, the cuts in the fiber necessary to make the inner-cladding ray trajectories chaotic also make coupling of the incoherent diode-bar pump into the modified cladding more difficult [See Fig. 2 of Ref. (10)].

In this paper, we show that a relatively small asymmetric deformation of the circular cladding achieves a similar effect. To our knowledge, all cladding shapes considered in the literature have at least one symmetry (mirror reflection). Any symmetry of the inner cladding favors periodic trajectories that can exhibit poor overlap with the core. One of the simplest asymmetric deformations is a spiral cladding, which is the main subject of this paper.

The spiral inner-cladding shape is not convex figured, and all modes must have significant amplitude in the vicinity of the deformation. The core placed in this region should have good overlap with all of these modes. One can therefore expect that the spiral shape will provide a high efficiency of absorption of the pump light in the core.

2. GENERALIZED AND APPROXIMATE IMAGES

The conventional beam propagation method¹² is severely limited as a wave optical propagation scheme over physi-

cally realistic distances for fibers with large inner cladding, cross section, and generally shaped inner cladding boundaries. The technique of approximate images (AI) was introduced in our earlier work as a computational method to simulate the propagation of complex spatially incoherent diode pump modes in an inner cladding of rather large cross sectional area over relatively long distances. The generalized image (GI) method is somewhat analogous to the method of images in electrostatics¹³ where an image of a point charge is placed at the other side of a conducting surface to ensure that the field on the surface is identically zero. Here, however, we do not treat point charges, but rather extended fields. As an illustration consider a cylindrically symmetric inner cladding and ignore the central core for the moment. The natural basis functions with which to describe an arbitrary optical field propagating in such a structure are Bessel modes. Other shapes of cladding yield different basis functions. We now assume that the inner-cladding-to-outer-cladding index step is so large that the field is essentially zero on the boundary. Alternatively, one can assume that the outer cladding is highly absorbing and hence acts as a reflecting surface. This is an approximation in any event. The requirement that the field be zero on the boundary enforces the selection of a finite set of Bessel modes that satisfy that criterion on the boundary at $\rho = R$, where R is the radius of the boundary and ρ is the radial coordinate. Figure 1 shows a graph of two such Bessel functions that are identically zero at the boundary $\rho = R$. We consider the part of the Bessel function defined on $0 \leq \rho \leq R$ as the physical field and its extension outside the boundary on $R \leq \rho \leq \infty$ as its GI. The GI field is denoted by the dotted curve in the figure. Formally we can propagate an arbitrary initial field distribution along this waveguide by simply propagating the appropriate combination of extended Bessel modes (such as shown in Fig. 1) in free space. This approach removes the outer-cladding boundary from explicit consideration. Practically, these Bessel modes extend far outside the inner-cladding boundary, and it becomes im-

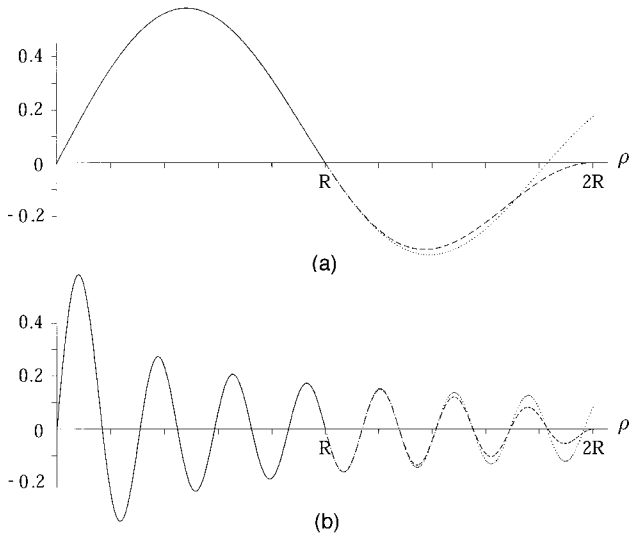


Fig. 1. Radial modes of a circular fiber in the absence of the core; (a) $J_1(3.831706\rho/R)$ and (b) $J_1(22.76008\rho/R)$. The solid curves depict the physically relevant inner cladding modes. Their extension (GI) outside of the cladding is depicted by the dotted curves and their AI [Eq. (5)] by the dashed curves.

practical to propagate these on a computer. The method of AI is designed to bypass this difficulty by constructing compactly supported functions as approximations to the GI in the vicinity of the cladding boundary. The dashed curve outside the inner-cladding boundary at $\rho = R$ for both the low- and high-order Bessel mode depicts such AI fields. One should note from the figure that the AI depiction is a better representation of the GI field for highly oscillatory Bessel modes. The explicit mathematical construction of these AI fields is shown below for the spiral and other inner cladding shapes.

The more general problem of a noncircular inner cladding is now considered, and a central doped core is now introduced explicitly in what would otherwise be an effective free-space-propagation problem. The core is treated as a small perturbation for the multimode pump, which is a physically realistic assumption. In particular, the refractive-index step in the core will be larger than the corresponding absorption per wavelength. In the paraxial approximation, the propagation of the pump can now be described by the equation

$$\dot{E} = \frac{i}{2k} \Delta_{\perp} E - ik\nu E - \mathcal{K}E, \tag{1}$$

where $E = E(x, y, z)$ is the complex field, dot denotes differentiation with respect to the last argument (longitudinal coordinate), Δ_{\perp} is the Laplacian with respect to the first two arguments (transverse coordinates), $k = 2\pi n_{\text{ref}}/\lambda$ is the wave number of the pump in the cladding with refractive index n_{ref} , $\nu = (n^2 - n_{\text{ref}}^2)/n_{\text{ref}}$ is the effective variation of the refractive index, and \mathcal{K} is the local absorption rate. As discussed above, the strong variation of the refractive index from inner to outer cladding can be taken into account with the boundary condition

$$\mathcal{E}(R(\phi), \phi) = 0, \tag{2}$$

where $\mathcal{E}(\rho, \phi) = E(\rho \cos \phi, \rho \sin \phi)$, and the function R parameterizes the surface of the cladding in polar coordinates.

We now outline the procedure for obtaining an AI field for this general problem. Consider Fig. 2. For any point (X, Y) of the crosssection of the fiber located outside of the inner cladding, the square of the distance to the point $[R(\phi)\cos \phi, R(\phi)\sin \phi]$ can be expressed with the function $F(\phi, X, Y)$ such that $F(\phi, X, Y) = (RC - X)^2 + (RS - Y)^2$, where $C = \cos \phi$, $S = \sin \phi$, $R = R(\phi)$. The closest point of the surface of the fiber (RC, RS) corresponds to the angular coordinate ϕ such that $F'(\phi, X, Y) = 0$, where the prime denotes differentiation with respect to the first argument. Then, the minimum of $F(\phi, X, Y)$ with respect to the first argument defines the function $\phi = \phi(X, Y)$ such that

$$RR' - (CX + SY)R' + (SX - CY)R = 0. \tag{3}$$

We suppose that the function R is smooth. The approximate solution ϕ_1 of Eq. (3) can be expressed as a first iteration of Newton's method: $\phi_1 = \phi_0 - F'(\phi_0)/F''(\phi_0)$. The choice of an AI field is not unique. First, calculations were done with an AI field represented by

$$\mathcal{E}_{AI} = -E(X_1, Y_1)[1 - (R - \rho)^2/\rho_0^2]\theta(R + \rho_0 - \rho), \tag{4}$$

for $\rho \geq R(\phi)$, where $X_1 = X_1(X, Y) = R(\phi_1)\cos \phi_1$, $Y_1 = Y_1(X, Y) = R(\phi_1)\sin \phi_1$, and $\theta(x) = (x + |x|)/2$. The parameter ρ_0 should be small enough to prevent instabilities of the numerical implementation. This AI is essentially a scaled inverted replica of the inner field. Calculations were then repeated with an improved AI field given by

$$\mathcal{E}_{AI} = -E(X, Y)W\theta(W), \tag{5}$$

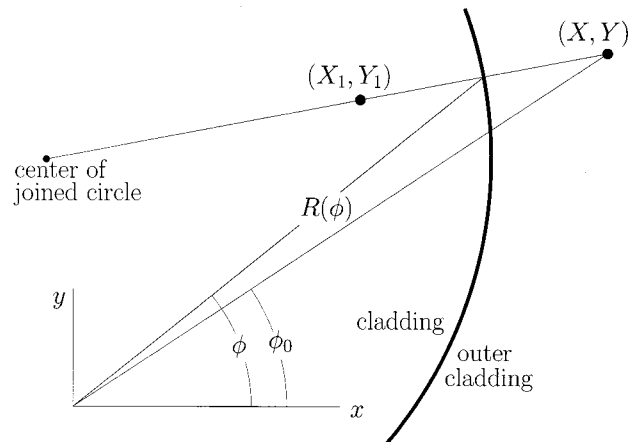


Fig. 2. Scheme of construction of the approximate image field $E_{AI}(X, Y)$ for a smooth boundary of a nonsymmetrical inner cladding.

where $W = W(X, Y) = (1 - D)[\rho - R(\phi)]$ scales of the AI, $D = D(\phi) = (R^2 + 2(R')^2 - RR'')/[R^2 + (R')^2]^{3/2}$ is the curvature of the inner-cladding boundary, and ϕ is the solution of Eq. (3). Formula (5) shows faster convergence of the numerical solution in comparison with Eq. (4) if we approximate $R(\phi)$ with an analytical function. The step of integration d_z can be increased by at least an order of magnitude while retaining the same error of the numerical method. Formula (16) of Ref. 9 is a special case of formula (5) above for $R(\phi) = \text{const}$. [Unfortunately, there is a mistake in Eq. (16) of Ref. 9; the last factor in the expression for the case $R < \rho \leq 2R$ appears as $(2R - \rho/R)$ instead of $(2R - \rho)/R$.]

3. SIMULATIONS

In this section, we describe numerical simulations for varying shapes of inner-cladding boundary. We employ an operator-splitting method somewhat akin to the split-step fast Fourier transform in the usual beam propagation method.¹² The operator f of the elementary step of propagation from z to $z + d_z$ can be constructed in analogy with Ref. 9 as the product $f = \Phi \mathcal{N} \mathcal{F}^\dagger \mathcal{P} \mathcal{F}$, where \mathcal{F} is the Fourier operator, \mathcal{P} is the propagation operator (diagonal in the Fourier representation), $\mathcal{N}E(x, y, z) = \exp[ik\nu(x, y)d_z]E(x, y, z)$ is the operator of refraction (diagonal in the coordinate representation), and the projector Φ substitutes the field outside of the cladding by the AI of the field inside.

We have made simulations with the following configurations of the cladding and the core:

- circular, $R(\phi) = R_0 = \text{constant}$;
- smooth spiral,

$$R(\phi) = \begin{cases} R_0 + \alpha_0 \phi, & |\phi| \leq \beta_0, \\ R_0 + \alpha_0 \text{sgn}(\phi) \left[\frac{\pi + \beta_0}{\pi - \beta_0} (\pi - |\phi|) - \frac{\pi}{(\pi - \beta_0)^2} (\pi - |\phi|)^2 \right], & |\phi| \geq \beta_0; \end{cases} \quad (6)$$

$$\text{starlike structure } R(\phi) = R_0 + \alpha_0 \cos 6\phi; \quad (7)$$

$$\text{squarelike structure } R(\phi) = R_0 - \alpha_0 \cos 4\phi. \quad (8)$$

Figure 3(a) shows the dependence of the efficiency of absorption of the pump versus dimensionless parameter $Z = \mathcal{K}_0 z$ for various cases of the geometry of the cladding and core placements. Some of these inner cladding shapes are shown in Fig. 4. The simulations use a wave number for the pump $k = 2\pi n_1/\lambda = 10 \mu\text{m}^{-1}$, the index of refraction of the core $n_1 = 1.56$, index of refraction of the cladding $n_2 = n_1 - 0.0033$, absorption rate in the core $\mathcal{K}_0 = 0.01 \mu\text{m}^{-1}$. The radius of the cladding $R_0 = 20 \mu\text{m}$ and the radius of the core $r = 4 \mu\text{m}$. A grid of 512×512 points was used, and the step d_x was chosen in such a way that this grid adequately resolves the internal field and its approximate image. In the case of the offset core, its coordinates were $(x_0, 0)$.

The upper dashed curve represents the analytic estimate for the case of ideal mixing of the pump, i.e.,

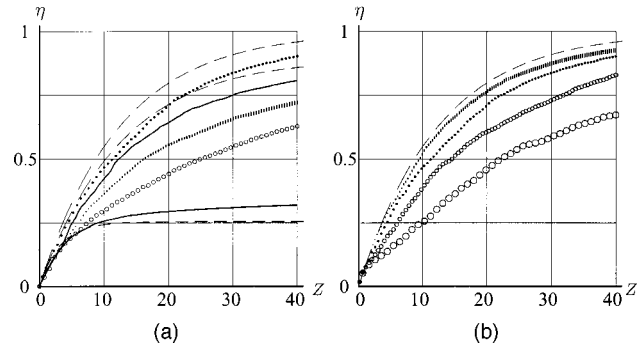


Fig. 3. (a) Efficiency η of absorption of the pump light in the core versus $Z = \mathcal{K}_0 z$. Upper dashed curve, case of ideal mixing [estimate by Eq. (9)]; dotted curve, simulation of spiral cladding with displaced core; intermediate dashed curve, the analytical estimate by formula (10); upper solid curve, numerical simulation for the same case; vertical bars, simulation for the starlike cross section; circles, simulation for spiral cladding with centered core; lowest solid curve, simulation for circular-symmetric case; lowest dashed curve, analytical estimation for the same case according to Eq. (11). (b) Efficiency of absorption of the pump light in the core of the offset-spiral double-clad fiber at $\mathcal{K}_0 = 0.005 \mu\text{m}^{-1}$, bars; $0.01 \mu\text{m}^{-1}$, dots; $0.02 \mu\text{m}^{-1}$ small circles; $0.04 \mu\text{m}^{-1}$, large circles; versus dimensionless Z .

$$\eta_{\text{ideal}} = 1 - \exp\left[-2\mathcal{K}_0\left(\frac{r_0}{R_0}\right)^2 z\right], \quad (9)$$

discussed in Refs. 9–11. This estimate is based on the assumption of a uniform distribution of the pump light intensity on the cross section of the inner cladding.

The initial condition for the numerical simulations was prepared in the same manner as in Ref. 9. We employed a maximal transversal wave number $p_{\text{max}} = 2 \mu\text{m}^{-1}$.

The projector Φ is applied in the sequence shown above. A filter is applied in Fourier space to eliminate spatial frequencies with transversal wave numbers greater than p_{max} . The whole process is repeated to advance the solution in z .

The lower solid curve represents the case of numerical simulations for a circular cladding with centered core ($d_x = 0.22 \mu\text{m}$, $d_z = 0.04 \mu\text{m}$, $\rho_0 = 6 \mu\text{m}$, $x_0 = 0$). As expected the coupling efficiency is low. We previously noted in Ref. 9 that random index perturbations in the inner cladding glass could significantly improve the coupling efficiency for this case. We expect that the deformation of the inner cladding should achieve an even stronger effect. The curve with open circles represents the numerical simulation for the spiral cladding with central core and with $R(\phi)$ given by Eq. (6). This relatively weak distortion from a circular cladding shape [see Fig. 4(d)] significantly enhances the coupling efficiency relative to the circular cladding with centered core. We used a 512×512 grid with step $d_x = 0.22 \mu\text{m}$, $d_z = 0.04 \mu\text{m}$, $\rho_0 = 6 \mu\text{m}$, $x_0 = -12 \mu\text{m}$, $\alpha_0 = 1 \mu\text{m}$, β_0

= 2.7 rad in these simulations. First, the simulations were carried out with the AI described by Eq. (4). Then, the simulations were repeated using the AI formula given by Eq. (5), and the same precision was achieved using a space step $d_z = 0.5 \mu\text{m}$. As the accuracy is the same the curves are indistinguishable and only one set is plotted.

The intermediate dashed curve (which crosses the dotted curve at $\mathcal{K}_0 z \approx 20$) represents the analytical estimate

$$\eta = \frac{2}{\pi} \left\{ \frac{r_0 + |x_0|}{R} \left[1 - \left(\frac{r_0 + |x_0|}{R} \right)^2 \right]^{1/2} + \arcsin \left(\frac{r_0 + |x_0|}{R} \right) \right\} \left\{ 1 - \exp \left[-2\mathcal{K}_0 \left(\frac{r_0}{R_0} \right)^2 z \right] \right\} \quad (10)$$

for the case of a circular cladding and an offset core [see Figure 4(b)], based on geometrical optics.^{8,9} The upper solid curve represents the numerical simulation for this same case ($d_x = 0.22 \mu\text{m}$, $d_z = 0.04 \mu\text{m}$, $\rho_0 = 6 \mu\text{m}$, $x_0 = -12 \mu\text{m}$).

The curve formed of vertical bars represents the numerical solution for the case of a fiber with starlike cross section with centered core given by Eq. (7) [see Fig. 4(c)] with $R_0 = 20 \mu\text{m}$, $\delta_r = 1 \mu\text{m}$, $d_x = 0.20 \mu\text{m}$, $d_z = 0.04 \mu\text{m}$, $\rho_0 = 4 \mu\text{m}$, $x_0 = 0$. (Due to the relatively fast oscillations of the function R , a value $\rho_0 = 6 \mu\text{m}$ caused an instability of the solution.) The upper extremum of each bar represents the calculation based on the total power of the field at a fixed plane, whereas the lower extremum corresponds to the calculation based on the in-

tegration of intensity of the field in the cross section of the cladding. The vertical height of the bars estimates the error of the approximation. In both Fig. 3(a) and Fig. 3(b), vertical bars are used for the curve with maximal error, which is $\sim 2\%$. The dots represent the numerical solution for the offset core in the spiral cladding ($d_x = 0.22 \mu\text{m}$, $d_z = 0.04 \mu\text{m}$, $\rho_0 = 6 \mu\text{m}$, $x_0 = -12 \mu\text{m}$, $\alpha_0 = 1 \mu\text{m}$, $\beta_0 = 2.7 \text{ rad}$). This configuration shows coupling efficiencies comparable to or stronger than those of the double-truncated circular fiber discussed in Ref. 10.

The lowest dashed curve in Fig. 3(a) represents the analytic estimate

$$\eta = \frac{4r_0}{\pi R_0} \left[1 - \exp \left(-\mathcal{K}_0 \frac{\pi r_0}{2R_0} z \right) \right], \quad (11)$$

which is the limit case of Eq. (10) at $r_0/(|x_0| + r_0) \ll 1$. For this case, it practically coincides with the estimate given by Eq. (10).

The offset-spiral double-clad fiber shows the best coupling efficiency of all cases considered. Figure 3(b) shows how the coupling efficiency varies with core absorption for this offset-spiral double-clad fiber. Coupling efficiencies are shown for absorption rates $\mathcal{K}_0 = 0.005 \mu\text{m}^{-1}$ (bars), $\mathcal{K}_0 = 0.01 \mu\text{m}^{-1}$ (dots), $\mathcal{K}_0 = 0.02 \mu\text{m}^{-1}$ (small circles), and $\mathcal{K}_0 = 0.04 \mu\text{m}^{-1}$ (large circles). We use the parameter values $r_0 = 4 \mu\text{m}$, $R_0 = 20 \mu\text{m}$, $\delta_n = 0.0033$, $k = 10 \mu\text{m}^{-1}$, $\rho_0 = 6 \mu\text{m}$; $R(\phi)$ is given by Eq. (6) at $\alpha_0 = 1 \mu\text{m}$, $\beta = 2.7 \text{ rad}$. Again, we used a 512×512 grid with step $d_x = 0.20 \mu\text{m}$. For the first curve (bars) d_z

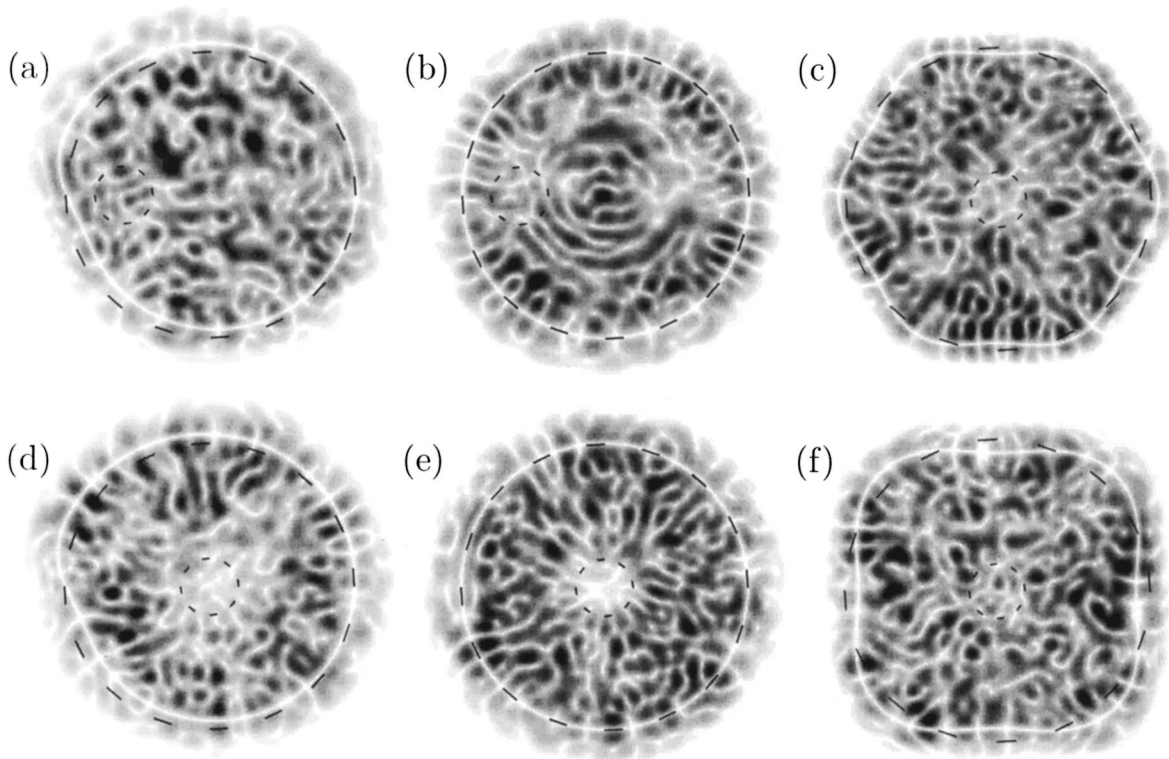


Fig. 4. Final distributions of amplitude of the field E after propagation of distance such that $\mathcal{K}_0 z = 40$. (a) Spiral cladding, offset core; (b) Circular cladding with offset core; (c) Cladding with the starlike cross section according to Eq. (7); (d) Spiral cladding, centered core; (e) Circular cladding, centered core; (f) Smoothed square cladding according to Eq. (8), centered core.

$= 0.02 \mu\text{m}$; $d_z = 0.04 \mu\text{m}$ for other cases. The upper (dashed) curve and the dotted curve are the same as in Fig. 3(a).

Figure 4 represents the final distribution of the amplitude of the field and its AI in the cases of fibers of displaced spiral (a), displaced circular (b), smooth star (c), centered spiral (d), centered circular (e), and smooth square (f) shapes. The density of shading is proportional to the square root of the amplitude of the field. On such a scale, details of the spots of low intensity are seen better than in a plot of the intensity of the field. Small dashed circles indicate the core. For a proper perspective, the circle of radius R_0 is drawn as a large dashed circle in each case. For the circular cladding, this circle coincides with the cross section of the surface of the cladding.

We see, in the case with circular cladding and offset core [(b)], that the pump light is partially depleted not only in the area of the core, but also in the symmetric point at the right side. This does not happen in the case of the smooth spiral cladding.

Analytical estimations of Eqs. (9), (10), and (11) depend only on $Z = \mathcal{K}_0 z$ but do not depend on \mathcal{K}_0 and z separately. The good fit (within a few percent) of the bars and the dashed curve in Fig. 3(b) shows good coupling of the pump into the core in the case of a small spiral distortion. However, the good fit also indicates that results of the simulations above can be extrapolated to the case of smaller and more realistic values of \mathcal{K}_0 . The proportionality of the local absorption rate and the effective absorption rate indicate that the efficiency of coupling of the power of the pump light into the core can be precisely estimated in the first order of perturbation theory borrowed from nonrelativistic quantum mechanics. This possibility is exploited in Ref. 14.

4. CONCLUSIONS

Small spiral deformations of a circular cladding significantly improve the coupling of the pump power into the core, providing the same effect as a strong double-cut inner cladding.^{10,11} At moderate values of the local absorption rate $\mathcal{K}_0 < 100 \text{ cm}^{-1}$ in the offset core, the effective absorption rate is almost proportional to the local absorption rate and approaches the fundamental limit of the ideal mixing of the pump.

ACKNOWLEDGMENTS

The authors thank Ewan M. Wright, Robert M. Indik, Miroslav Kolesik, and other colleagues of Arizona Center

for Mathematical Sciences for useful discussions and help given. This work was supported by Air Force Office of Scientific Research grants F49620-00-1-0002 and F49620-00-1-0190 and, in part, by a National Science Foundation Grant opportunities for Academic Liaison with Industry Division of Mathematical Sciences 9811466.

D. Kouznetsov's e-mail address is dima@acms.arizona.edu.

REFERENCES

1. K. Ueda and A. Liu, "Future of high-power fiber lasers," *Laser Phys.* **8**, 774–781 (1998).
2. V. Dominic, S. MacCormack, R. Waarts, S. Sanders, S. Bicknese, R. Dohle, E. Wolak, P. S. Yeh, and E. Zuker, "110W fiber laser," *Electron. Lett.* **35**, 1158–1160 (1999).
3. V. Karpov, W. R. L. Clements, E. M. Dianov, and S. B. Papernyi, "High-power 1.48 μm phosphoro-silicate-fiber-based laser pumped by laser diodes," *Can. J. Phys.* **78**, 407–413 (2000).
4. N. S. Kim, T. Hamada, M. Prabhu, C. Li, J. Song, K. Ueda, A. P. Liu, and H. J. Kong, "Numerical analysis and experimental results of output performance for Nd-doped double-clad fiber lasers," *Opt. Commun.* **180**, 329–337 (2000).
5. C. K. Liu, F. S. Lai, and J. J. Jou, "Analysis of nonlinear response in erbium-doped fiber amplifiers," *Opt. Eng.* **39**, 1548–1555 (2000).
6. M. A. Mahdi, S. Thirumeni, P. Poopalan, S. Selvakennedy, F. R. M. Adikan, W. Y. Chan, and H. Ahmad, "Effects of self-saturation in an erbium-doped fiber amplifier," *Opt. Fiber Technol. Mater., Devices Syst.* **6**, 265–274 (2000).
7. S. Bedö, W. Lüthy, and H. P. Weber, "The effective absorption coefficient in double-clad fibers," *Opt. Commun.* **99**, 331–335 (1993).
8. A. Liu and K. Ueda, "The absorption characteristics of circular, offset, and rectangular double-clad fibers," *Opt. Commun.* **132**, 511–518 (1996).
9. D. Kouznetsov, J. V. Moloney, and E. M. Wright, "Efficiency of pump absorption in double-clad amplifiers. I. Fiber with circular symmetry," *J. Opt. Soc. Am. B* **18**, 743–749 (2001).
10. V. Doya, O. Legrand, and F. Mortessagne, "Optimized absorption in a chaotic double-clad fiber amplifier," *Opt. Lett.* **26**, 872–874 (2001).
11. V. Doya, "Du SPECKLE au SCARS: une expérience de chaos ondulatoire dans une fibre optique," Ph.D. Thesis (École Doctorale, Sciences et Technologies de l'Information et de la Communication, Université de Nice-Sophia Antipolis, France, December 12, 2000).
12. A. Newell, J. V. Moloney, *Nonlinear Optics* (Addison-Wesley, New York, 1992).
13. J. D. Jackson, "Boundary values problems in electrostatics," in *Classical Electrodynamics* (Wiley, New York, 1999), p. 57.
14. D. Kouznetsov and J. V. Moloney, "Efficiency of pump absorption in double-clad amplifiers. III. Calculation of modes," *J. Opt. Soc. Am. B* **19**, 1304–1309 (2002).